



Studies on the performance of functionalized Fe₃O₄ as phosphate adsorbent and assessment to its environmental compatibility

Artik Elisa Angkawijaya^{a,*}, Yen Nhi Tran-Chuong^{b,†}, Quoc Nam Ha^{b,†},
Phuong Lan Tran-Nguyen^c, Shella Permatasari Santoso^{d,b}, Vania Bundjaja^b, Alchris Woo Go^a,
Hsien-Yi Hsu^{e,f}, Yi-Hsu Ju^{a,b,g}

^a Graduate Institute of Applied Science, National Taiwan University of Science and Technology, #43, Sec. 4, Keelung Rd., Taipei, Taiwan

^b Department of Chemical Engineering, National Taiwan University of Science and Technology, #43, Sec. 4, Keelung Rd., Taipei, Taiwan

^c Department of Mechanical Engineering, Can Tho University, 3/2 Street, Can Tho City, Vietnam

^d Department of Chemical Engineering, Widya Mandala Surabaya Catholic University, Kalijudan 37, Surabaya, Indonesia

^e School of Energy and Environment & Department of Materials Science and Engineering, City University of Hong Kong, Kowloon Tong, Hong Kong, China

^f Shenzhen Research Institute of City University of Hong Kong, Shenzhen, China

^g Taiwan Building Technology Center, National Taiwan University of Science and Technology, #43, Sec. 4, Keelung Rd., Taipei, Taiwan

ARTICLE INFO

Article History:

Received 14 September 2021

Revised 9 November 2021

Accepted 22 November 2021

Available online 12 December 2021

Keywords:

eutrophication
phosphate removal
thiamine
magnetic iron oxide
adsorption
plant growth

ABSTRACT

Background: The pressing demand to increase agricultural productivity amid the rapidly growing population has exponentially boosted fertilizers usage. Phosphate (Pi) runoff from fertilizers induces eutrophication in water sources and severely affects its surrounding ecosystems. To cope with Pi accumulation problem, this study reported the synthesis of an environmentally friendly magnetic adsorbent, namely Fe₃O₄/thiamine (thF).

Method: A one-step chemical oxidation and functionalization technique for thF synthesis was developed. X-ray diffraction (XRD), X-ray photoelectron spectroscopy (XPS), Fourier-transform infrared spectroscopy (FTIR), nitrogen (N₂) sorption, and superconducting quantum interference device (SQUID) analysis were conducted to ensure the formation of Fe₃O₄, confirm the successful incorporation of thiamine, and gain insight into the factors influencing the adsorptivity of thF-363.

Significant Findings: The thF synthesized at 363 K (thF-363) produces an adsorbent with the highest Pi removal efficiency compared to other synthesis conditions. The thF-363 showed up to 1.51-fold higher adsorption capacity than the unmodified Fe₃O₄. The large surface area and occurrence of thiamine functional groups are the contributing factors in enhancing its adsorption capacity for Pi removal. The thF-363 did not adversely affect the growth of the model plant, *Arabidopsis thaliana*; demonstrating its suitability as an environmentally friendly adsorbent for Pi removal from eutrophicated water with the feasibility of magnetic separation from an aqueous system.

© 2021 Taiwan Institute of Chemical Engineers. Published by Elsevier B.V. All rights reserved.

1. Introduction

Phosphorus in phosphate (Pi) form is essential for every organism, including humans, animals, and plants. Appropriate Pi intake is majorly related to bone–teeth health and overall growth for animals and humans [1]. Similarly, Pi availability is also affiliated to plant vigor, where Pi deficiency had been acknowledged to affect root growth. The prolonged starvation eventually can be detrimental to the sustainability of agriculture [2,3]. Due to its indispensable nature,

most global Pi consumption is allocated for the production of fertilizers and animal feed supplements [4,5]. Pi-fertilizers are regularly applied on agricultural soil to maintain adequate-high levels of Pi to satisfy the plant demand for growth and development. However, only less than half of the administered Pi is absorbed by crops while the remainder is leached to the environment through soil and often end-up in water [6,7]. Accumulation of Pi in the water body had been acknowledged as the primary cause of eutrophication which sets off a series of detrimental effects in the aquatic ecosystem; from the algal bloom to the generation of hypoxic or anoxic ‘dead zone’ which affect the availability of oxygen in water [8]. To alleviate this issue, various methods such as chemical precipitation, biological treatment, anion exchange, electro-coagulation, acid-thermal treatment, and adsorption have been developed to efficiently remove

* Corresponding Author: Artik Elisa Angkawijaya, Graduate Institute of Applied Science, National Taiwan University of Science and Technology

E-mail addresses: artikelisa@mail.ntust.edu.tw, artikelisa@yahoo.com

(A.E. Angkawijaya).

† These authors contribute equally.

excess Pi from water resources [9–16]. Among them, adsorption is one of the most used methods in managing Pi concentration in water, owing to its inexpensive and straightforward operation.

Several composite adsorbents prepared from a combination of inorganic and organic compounds had been widely used for Pi removal application. For instance, MgO/biochar possessed Pi adsorption capacity up to 122 mg/g [17], the adsorption capacity of montmorillonite-iron crosslinked alginate, and its zirconium modified alginate can reach 48.78 mg/g and 67.72 mg/g, respectively [18,19]. While various adsorbents with excellent adsorption capacity for Pi removal had been developed, separation of the post-adsorption adsorbent from the water is the main issue that leads to the impracticability of those adsorbents. Filtration and/or centrifugation procedure are commonly performed to recover the adsorbent from treated water. In this work, an adsorbent with magnetic-separability property was developed, with Fe₃O₄ as the core material. Superparamagnetic Fe₃O₄ possesses remarkable magnetic properties that allow its practical separation post-adsorption using an external magnetic field [20–22]. Besides their superparamagnetic and adsorbing properties, the low toxicity, durability, biocompatibility, low cost, and chemical stability of Fe₃O₄ made them the promising adsorbent for water treatment [23–26].

In this study, a composite material consisting of Fe₃O₄ and thiamine was developed to generate magnetic adsorbent with enhanced adsorption capacity. Thiamine, also known as Vitamin B1, is a water-soluble vitamin beneficial for plants and animals due to its antioxidant activity. It may also function as a cofactor for various metabolic activities [27,28]. In plants, thiamine is distributed in leaves, seeds, flowers, and roots; and is known to play a role to protect plant from abiotic and biotic stresses [29,30]. Thiamine molecule consists of a pyrimidine ring (4-amino-2-methyl-5-pyrimidyl) which is connected to a thiazole ring (4-methyl-5-β-hydroxyethylthiazolium) through a methylene bridge [31]. The occurrence of these N-functional groups in thiamine, which tends to be positively charged, is expected to promote the adsorption capacity toward anionic Pi ions [32–34]. In addition, through the beneficial effect of thiamine for plant stress adaptation, the post-adsorption thiamine-functionalized Fe₃O₄ (thF) can be a potential Pi-supplement to support plant growth. This study also investigated the effect of synthesis temperature on the product yield and its Pi-removal performance. Several physicochemical characterizations were carried out to elucidate the properties of thF, including crystallinity pattern, surface chemistry, surface functional groups, porosity, and magnetic behavior. The physicochemical properties of thF were compared to that of unmodified Fe₃O₄ (F) to confirm the successful incorporation of thiamine. Adsorption isotherm of Pi by thF and F at different temperatures was conducted to study their adsorption behavior and mechanism. The environmental compatibility of these adsorbents was also assessed.

2. Materials and methods

2.1. Materials

All chemicals used were of analytical grade and were used without any pretreatment. Iron(II) sulfate heptahydrate (FeSO₄·7H₂O, purity >99.5%) and hydrochloric acid (HCl, purity 37%) were purchased from Acros Organics, New Jersey, USA. Ammonia (NH₃, purity 28–30%) and potassium dihydrogen phosphate (KH₂PO₄, purity ≥99.5%) were manufactured by Showa, Tokyo, Japan. Thiamine hydrochloride (C₁₂H₁₇ClN₄OS.HCl, purity ≥99%) was a product of Sigma, St.Louis, MO, Germany. Sodium hydroxide (NaOH, purity >97%) was obtained from Fisher Scientific, Loughborough, UK. The solutions used for the experiments were freshly prepared before use by dissolving a certain amount of chemicals in deionized (DI) water with 18.3 MΩ·cm.

2.2. Synthesis of magnetite-based adsorbent

For thF synthesis, 0.2024 g of thiamine and 0.1668 g of FeSO₄·7H₂O (Fe salt) were dissolved in 20 mL of DI water. The solution was left to react for 1 h under constant mixing at 300 rpm at certain temperatures, as listed in Table 1. Subsequently, ammonia was added (molar ratio of NH₄OH, Fe salt, and thiamine 10:1:1). The mixture was then left to react for another hour. The precipitate generated from the reaction was magnetically separated from the supernatant with an external magnetic force. The pH of the supernatants was determined by Denver Instrument UltraBasic pH Benchtop Meters UB-10 and was presented as the solution pH at the end of the reaction (Table 1). On the other hand, the solid product was washed at least 3 times with DI water and ethanol and dried at 313 K under vacuum for 24 h. The unmodified Fe₃O₄ was prepared using a similar procedure, without the addition of thiamine, and used as a control.

2.3. Characterization

Thermogravimetric analysis (TGA) was performed using a TA instruments/TGA 550, operated at a temperature range of 303–973K with a heating rate of 10 K/min under N₂ flow. The crystal pattern of the prepared magnetite nanoparticles (thFs and Fs) was analyzed by a Bruker D2 Phaser X-ray diffractometer (XRD) using Cu-Kα radiation operating at 30 kV and 10 mA. Fourier-transform infrared spectroscopy (FTIR) analysis was performed on a Shimadzu IRTracer-100. The oxidation states of Fe element in the samples were determined using an X-ray photoelectron spectroscopy (XPS, Thermo Fischer Scientific, VG ESCALAB 250). The magnetic properties were measured by a superconducting quantum interference device (SQUID, MPMS 3) at 300 K. Surface area and pore properties were determined by N₂ adsorption-desorption isotherm procedure using a BEL Belsorp Max

Table 1

Synthesis temperature used and its influence on yield and Pi removal ability of the synthesized materials. Data are means ± SD from three replicates.

Sample name	Temp (K)	pH*	Yield _{Fe} ** (%)	Yield _{Fe+thiamine} *** (%)	% Removal
thF-303	303	9.24	31.00 ± 1.39 ^{ac}	14.00 ± 0.64	17.09 ± 1.76
thF-333	333	9.14	30.04 ± 0.55 ^{ab}	13.57 ± 0.25	34.37 ± 0.88
thF-363	363	9.11	33.93 ± 1.02 ^a	15.01 ± 0.46	48.33 ± 1.06
F-303	303	9.98	29.44 ± 0.55 ^{bc}		3.92 ± 0.49
F-333	333	9.92	27.16 ± 0.51 ^{bd}		5.82 ± 0.46
F-363	363	9.83	25.72 ± 0.30 ^d		7.67 ± 0.18

* pH of solution at the end of the reaction.

** The amount of product formed per amount of FeSO₄·7H₂O reactant used, calculated as Yield_{Fe} = $\frac{m_{\text{product}}}{m_{\text{FeSO}_4 \cdot 7\text{H}_2\text{O}}} \times 100\%$.

*** The amount of product formed per amount of FeSO₄·7H₂O and thiamine reactants used, calculated as Yield_{Fe+thiamine} = $\frac{m_{\text{product}}}{m_{\text{FeSO}_4 \cdot 7\text{H}_2\text{O}} + m_{\text{thiamine}}} \times 100\%$.

analyzer. Prior to the sorption experimentation, the samples were degassed at 393 K for 4 h. The N₂ adsorption-desorption data (V_a vs $\frac{p}{p_0}$) were then fitted with Brunauer–Emmett–Teller (BET) model, with mathematical expression shown in equation (1).

$$\frac{p}{V_a(p_0 - p)} = \frac{1}{V_m c} + \frac{c - 1}{V_m c} \left(\frac{p}{p_0} \right) \quad (1)$$

where V_m (cm³(STP)/g) and V_a (cm³(STP)/g) are the gas volume at the monolayer coverage and the total gas volume adsorbed at the standard state (T= 273.15 K and P= 101.3 kPa), c is the BET constant and $\frac{p}{p_0}$ (kPa) is the relative pressure. The obtained V_m value was then utilized to calculate the BET surface area ($a_{s,BET}$, cm²/g) by the following equation (2).

$$a_{s,BET} = \frac{V_m N A_{CS}}{22414} \quad (2)$$

where N is the Avogadro's number (6.023×10^{23} mol⁻¹), A_{CS} (cm²) is adsorbate cross-sectional area (16.2×10^{20}), 22414 cm³(STP)/mol is the molar volume of gas at STP. The total pore volume (V_p , cm³/g) and the mean pore diameter (d_p , nm) was determined by equations (3) and (4), respectively.

$$V_p = \frac{V M}{22414 \times \rho_a} \quad (3)$$

$$d_p = \frac{4 \times V_p}{a_{s,BET}} \times 1000 \quad (4)$$

where V (cm³(STP)/g) is amount N₂ adsorbed at last adsorption point, ρ_a is the density of adsorptive (0.808 g/cm³), and M is the nitrogen molecular weight (28.0134 g/mol).

The point of zero charge (pH_{PZC}) determination was done according to the reported procedure [35]. In brief, 10 mg of adsorbent was added into a series of 10 mL KNO₃ 0.1 M solution with initial pH between 2 to 10. The initial pH of these KNO₃ solutions was adjusted by HCl 0.1 M or NaOH 0.1 M. Subsequently, the mixture solution was placed on a shaking incubator (200 rpm) at 303 K. After 36 h incubation, the supernatants were collected and were used for final pH determination. The Δ pH was calculated by subtracting the value of the final pH from the initial pH. The pH_{PZC} of each particle is the pH where Δ pH equal to 0.

2.4. Adsorption Study

A 10,000 mg/L Pi stock solution was prepared by dissolving 10 g of KH₂PO₄ in 1 L of DI water. The diluted Pi solution was then prepared from the stock solution and was used for the adsorption experiment. The residual concentration of Pi solution post-adsorption was measured by a colorimetric procedure using a UV-Vis spectrophotometer Shimadzu UV 2600. The Pi solution was filtered using a 0.22 μ m PVDF syringe filter membrane prior to the colorimetric measurement. To these filtered solutions, ammonium molybdate-based reagent was added to produce a blue-colored solution which absorbance was measured at 880 nm wavelength [36].

2.4.1. Screening of Pi adsorption potential

Adsorbent (10 mg) was added into 10 mL Pi solutions at an initial concentration of 100 mg/L, the adsorption process lasted for 24 h under constant shaking at 200 rpm, and a temperature of 303 K. After 24 h, the adsorbent was magnetically separated from the supernatant, and the concentration of Pi that remained in the supernatant was measured.

2.4.2. Effect of pH on Pi adsorption

The effect of pH on Pi removal was investigated between pH range of 2 to 10. NaOH (0.1 M) or HCl (0.1 M) was used to adjust the initial pH of the Pi solution ($C_0 = 100$ mg/L). Into the 10 mL Pi solution,

10 mg adsorbent was added, and the mixtures was then placed in a shaking incubator at 200 rpm and 303 K. After 24 h, the supernatant was separated, and the amount of residual Pi that remained in the supernatant was measured.

2.4.3. Adsorption isotherm

The adsorption of Pi by the samples was conducted at pH 3 and 4 for F-363 and thF-363 samples, respectively. A series of 10 mL Pi solutions at a varied concentration (50 to 10,000 mg/L) were prepared in scintillation vials, then 10 mg of the sample was added. These vials were then placed in a shaking incubator, which operated at 200 rpm under a controlled temperature of 303, 318, or 333K. After 24h, residual Pi in the supernatant was measured.

2.4.4. Data processing

The percent removal of Pi (% Removal) and the equilibrium amount of Pi adsorbed per unit mass of adsorbent (Q_e) were calculated based on the equations (5) and (6), respectively.

$$\% \text{Removal} = \frac{(C_0 - C_e)}{C_0} \times 100\% \quad (5)$$

$$Q_e = \frac{(C_0 - C_e)}{m} \times V \quad (6)$$

where C_0 (mg/L) and C_e (mg/L) are the initial and equilibrium concentration of Pi, V (L) is the volume of the solution, and m (g) is the mass of adsorbents.

The adsorption data were plotted as Q_e vs C_e and were fitted against the Langmuir and Freundlich model, which is mathematically expressed as equations (7) and (8), respectively. These two models are used to respectively describe the monolayer and multilayer adsorption process that might occur during the adsorbate-adsorbent interaction [37].

$$Q_e = \frac{Q_L K_L C_e}{1 + K_L C_e} \quad (7)$$

$$Q_e = K_F C_e^{1/n_F} \quad (8)$$

where Q_L (mg/g) is the Langmuir maximum adsorption capacity, K_L (L/mg) is the Langmuir adsorption equilibrium constant, K_F (mg/g)(L/mg)^{1/n_F} is Freundlich isotherm constant related to adsorption capacity, and n_F is a dimensionless constant related to the favorability of adsorption. Furthermore, the suitability of adsorbents for Pi adsorption was evaluated from the value of the constant separation factor (R_L) obtained from the following equation (9).

$$R_L = \frac{1}{1 + K_L C_0} \quad (9)$$

Besides the model mentioned above, the Sips three-parameters model was employed for the data fitting purpose. This model is a modified form of the Freundlich equation, which follows the continuous increase of capacity as an increase of concentration but has a finite limit at the sufficiently high concentration [38]. The mathematical expression of the Sips model is given in equation (10).

$$Q_e = \frac{Q_S K_S C_e^{n_S}}{1 + K_S C_e^{n_S}} \quad (10)$$

where Q_S is the Sips maximum adsorption capacity (mg/g), K_S is the Sips equilibrium constant related to the adsorption affinity (L/mg), and n_S is the Sips model exponent that expresses the heterogeneity of the adsorbent. Sips model reduces to Langmuir model as the $n_S = 1$ and reduces to Freundlich when either C_e or $K_S \rightarrow 0$. These isotherm models were fitted with the experimental data gathered to evaluate the adsorption mechanisms to better understand how adsorbates interact with adsorbents. The linear regression (LR), nonlinear regression (NLR), and orthogonal distance regression (ODR) analyses

[39, 40] were performed by minimizing the sum of the squares of the residuals/error (SSE, equation 11) while the model coefficients were iteratively modified. The LR and NLR analyses were carried out using Microsoft Excel equipped with Solver data analysis tool pack with the regression results assessed through the resulting coefficient of determination (R^2 , equation 12), adjusted R-squared (R_{adj}^2 , equation 13), while the ODR analysis was conducted with the Origin2019 software.

$$SSE = \sum_{i=1}^n (Q_e - \widehat{Q}_e)^2 \quad (11)$$

$$R^2 = 1 - \frac{\sum_{i=1}^n (Q_e - \widehat{Q}_e)^2}{\sum_{i=1}^n (Q_e - \overline{Q}_e)^2} \quad (12)$$

$$R_{adj}^2 = 1 - \frac{(1 - R^2)(n - 1)}{n - k - 1} \quad (13)$$

where \widehat{Q}_e is the fitted value of equilibrium amount of Pi adsorbed per unit mass of adsorbent (mg/g), \overline{Q}_e is the average mean value of the equilibrium amount of Pi adsorbed per unit mass of adsorbent (mg/g), n is the number of experimental data points, and k is the number of parameters in the model, including the equilibrium concentrations predicted.

The thermodynamic parameters, i.e. the change in Gibbs free energy (ΔG°), enthalpy (ΔH), and entropy (ΔS), were based on the equations (14) to (17) [41].

$$\Delta G^\circ = -RT \ln K_d \quad (14)$$

$$\Delta G^\circ = \Delta H - T\Delta S \quad (15)$$

$$\ln K_d = -\frac{\Delta H}{RT} + \frac{\Delta S}{R} \quad (16)$$

$$K_d = 55.51 \times K_L \times 1000 \times MW_{adsorbate} \quad (17)$$

where K_d is the thermodynamic equilibrium constants dimensionless of the adsorption process [42]. R is the gas constant (8.314 J/mol.K) while T is the absolute temperature (K). By plotting $\ln K_d$ versus $1/T$, the change in ΔH , ΔS , and ΔG° can be obtained.

2.5. Arabidopsis thaliana growth media supplementation

To assess the environmental compatibility of the F-363 and thF-363, the freshly synthesized materials were administered to the plant growth media [43]. *A. thaliana* Col-0 ecotype was used as the model plant. The half-strength Murashige and Skoog (MS) basal medium supplemented with 1% (w/v) sucrose, 0.8% (w/v) agar media was prepared according to previous publications [3,44-46]. For the F-363 or thF-363 treatment group, 0.1 wt.% of respective materials were added into the basal media. The *A. thaliana* seeds were germinated and grown under continuous light condition at 295 K. After 14 days of vertical growth, the aerial fresh weight and primary root length of the seedlings were measured. Three independent biological experiments with 8 seedlings per replicate were performed for control, F-363, and thF-363-treated samples. Statistical analysis was conducted using the GraphPad Prism 8.0 software, and significant differences between different growth media compositions were examined by one-way analysis of variance (ANOVA) with Tukey's posthoc test.

3. Results and Discussion

This study employed three synthesis temperatures (303, 333, and 363 K) for thFs and Fs preparation. To ensure that the suitability of these conditions, firstly, the thiamine thermal stability was tested. As

shown in Figure S1, a negligible amount of % mass loss ($\sim 0.19\%$) of thiamine was observed upon 2 h isothermal heating at 363 K (the highest temperature used for the synthesis), which implies that the thiamine remained stable and did not undergo thermal degradation during the synthesis process.

The formation of thFs appears to depend on temperature, as implied from the increase in yield as the reaction temperature was increased (Table 1). The increase of synthesis temperature from 303 K to 333 K resulted in the decrease of thF Yield_{Fe} from 31.00% to 30.04%. However, the Yield_{Fe} was increased from 30.04% to 33.93% as the synthesis temperature increased from 333 K to 363 K. The increase in synthesis temperature shows a favorable effect on the formation of thF, which could be attributed to the high energy supply at higher temperature, thus facilitating the formation of thF. The supply of energy was reported to affect the nucleation rate in the formation of metal-organic complexes [47,48], which could also be the case in the formation of thF involving the interaction between thiamine and Fe₃O₄. Meanwhile, the higher thF-303 Yield_{Fe} (compared to Yield_{Fe} of thF-333) was attributed to the generation of side product FeO(OH); as shown by the occurrence of two additional XRD peaks at 2θ of 20.81° and 40.21° (Figure S2a), which were attributed to the reported (220) and (420) crystal plane of FeO(OH) (JCPDS No. 01-077-0247) [49,50]. Interestingly, no contaminant peaks were observed in thF-333 and thF-363 samples (Figures S2b and 1a).

Besides yield, the synthesis temperature was shown to positively affect the Pi removal efficiency of the resultant thFs, and the highest % Pi removal was achieved upon the usage of thF-363 as the adsorbent. This enhanced adsorption potential might be attributed to the higher composition of thiamine in thF prepared at 363K than the one synthesized at 333K. The TGA plots (Figure S2d and e) confirmed that the thF-363 contained approximately 15.16% thiamine, while only $\sim 6.94\%$ of the thF-333 consisted of thiamine. The higher thiamine content in thF-363 provides more adsorption sites for better Pi removal. The proposed interaction between the thF-363 and Pi is described in subsection 3.3. Based on the above-mentioned results, thF-363 has better Pi removal efficiency and higher Yield_{Fe} than thF-303 and thF-333; thus, detailed characterization and Pi adsorption studies were carried out for thF-363 and F-363 (as the control).

3.1. Characterization of thF-363

Figure 1a shows the crystal pattern of F-363 and thF-363; both samples had seven distinct diffraction peaks at similar 2θ angles, and these XRD patterns match well with the XRD pattern of Fe₃O₄ reference (JCPDS 19-0629), indicating the successful formation of Fe₃O₄ particles. The crystallinity of thF-363 was 57.8%, which is significantly lesser than the F-363 (81.2%). This reduced crystallinity can be attributed to the incorporation of thiamine on the magnetite core. The formation of Fe oxide was also confirmed by the occurrence of Fe-O functional group at $\sim 576 \text{ cm}^{-1}$ and $\sim 573 \text{ cm}^{-1}$ in the thF-363 and F-363 FTIR spectra (Figure 1b). Beside the Fe peak, thiamine fingerprint spectra, specifically the N-H group (3314 cm^{-1}), C-H aliphatic group (2922 cm^{-1}), aromatic amine C-N group (1652 cm^{-1}), C=C group (1524 cm^{-1}), C-S group (1325 cm^{-1}), and C-O group (1037 cm^{-1}) can be observed in the FTIR spectra of thF-363 which verify the formation of thiamine-functionalized Fe₃O₄. XPS analysis was performed to investigate the elemental state of Fe ions in thF-363 and F-363. As shown in Figure 1c, three peaks of iron (Fe 2p) with binding energies at 710.8, 712.3, and 724.8 eV, respectively attributed to Fe³⁺ 2p_{3/2}, Fe²⁺ 2p_{3/2} and Fe 2p_{1/2}, can be observed in the XPS patterns of F-363 [51,52]. Similarly, the thF-363 samples also showed three Fe 2p-related XPS spectra with the binding energy of 710.7, 712.6, and 724.7 eV (Figure 1d). Based on the stoichiometric, the Fe²⁺:Fe³⁺ ratio of thF-363 and F-363 is shown to be 0.34:0.66 and 0.37:0.63, respectively. These ratios are comparable to the previously reported Fe₃O₄

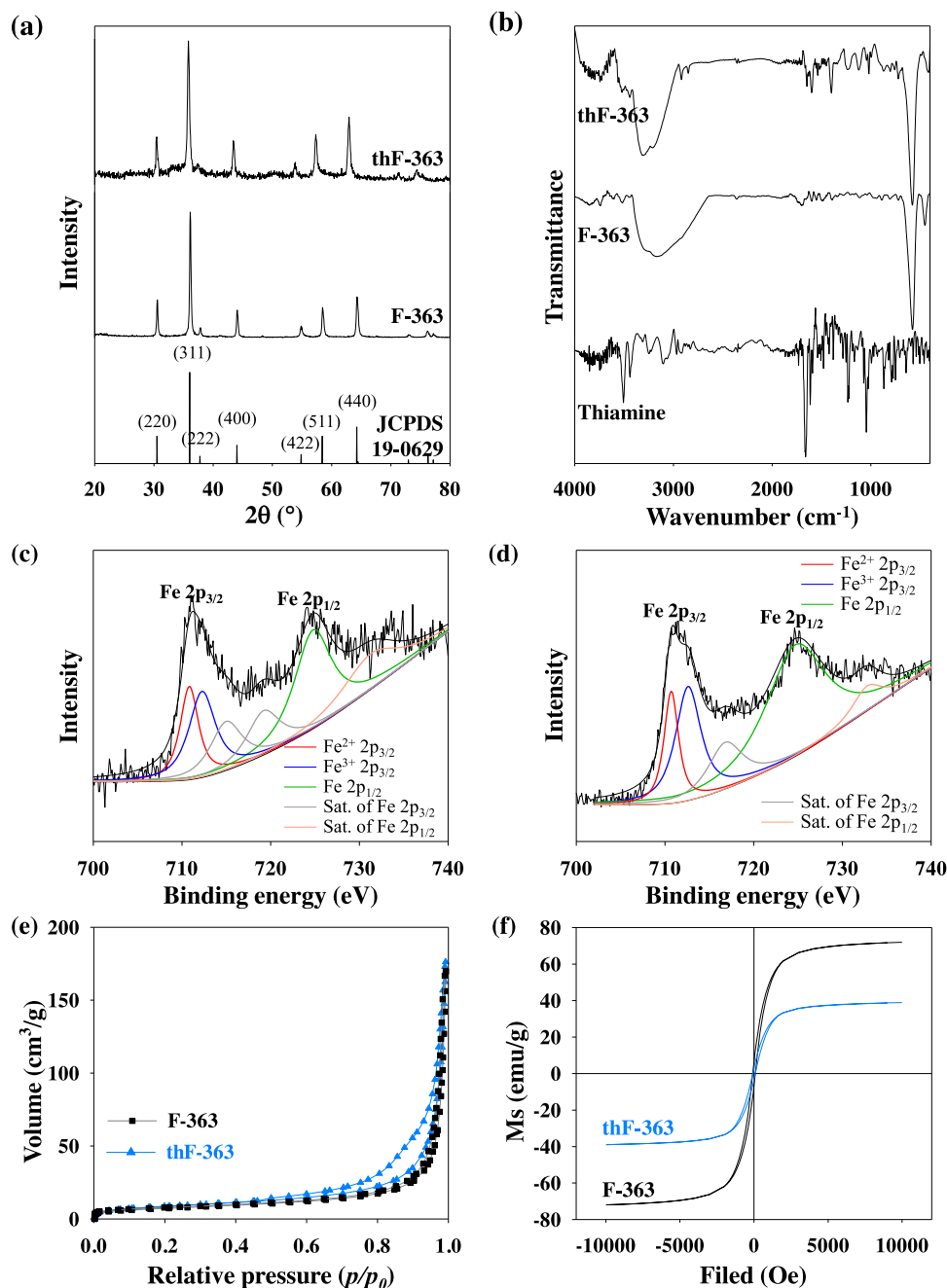


Figure 1. (a) Powder XRD pattern and (b) FTIR spectra of the thiamine-functionalized Fe_3O_4 synthesized at 363 K (thF-363) and control; unmodified Fe_3O_4 synthesized at 363 K (F-363). (c,d) The XPS spectra of (c) F-363 and (d) thF-363. (e) The N_2 adsorption-desorption isotherms curves and (f) hysteresis curves showing the magnetic properties of F-363 (black) and thF-363 (blue).

data [52], suggesting that the iron oxide in thF-363 and F-363 are in Fe_3O_4 form.

The N_2 adsorption-desorption isotherms of thF-363 and F-363 are shown in Figure 1e. According to IUPAC classification [53], the isotherm peak of both samples exhibited the type IV isotherms curve with H3-types hysteresis loop, which is commonly observed for mesoporous materials. Upon fitting by BET model, the d_p of thF-363 and F-363 is 32.913 nm and 36.976 nm, respectively, which is within the range of mesoporous material (2 to 50 nm). In addition, the thF-363 particles have an $a_{s,BET}$ of 32.999 m^2/g that is greater than that of the control (27.490 m^2/g). Figure 1f displays the magnetic hysteresis curves of thF-363 and F-363 measured at 300 K. The saturation magnetization values (M_s) of thF-363 and F-363 is 84.67 and 91.71 emu/g . Lower M_s value of thF-363 might be due to the addition of thiamine

which is non-magnetic. Despite the smaller M_s value, thF-363 (and F-363) fell into the classification of superparamagnetic material. Disregard of the reduced M_s , these values are postulated to be sufficient for magnetic recovery from solution [54].

3.2. Effect of initial pH on Pi adsorption

The influence of initial pH on the Pi removal by thF-363 and F-363 adsorbent was presented in Figures 2a and 2b. Optimum Pi removal by using thF-363 can be achieved when the initial pH of the adsorbate was set at pH 4. On the other hand, the efficiency of Pi removal by F-363 decreased upon increasing pH, and the optimum removal can be obtained between pH 2-3. The pH for Pi adsorption is essentially concentrated at low pH for both samples, which can be

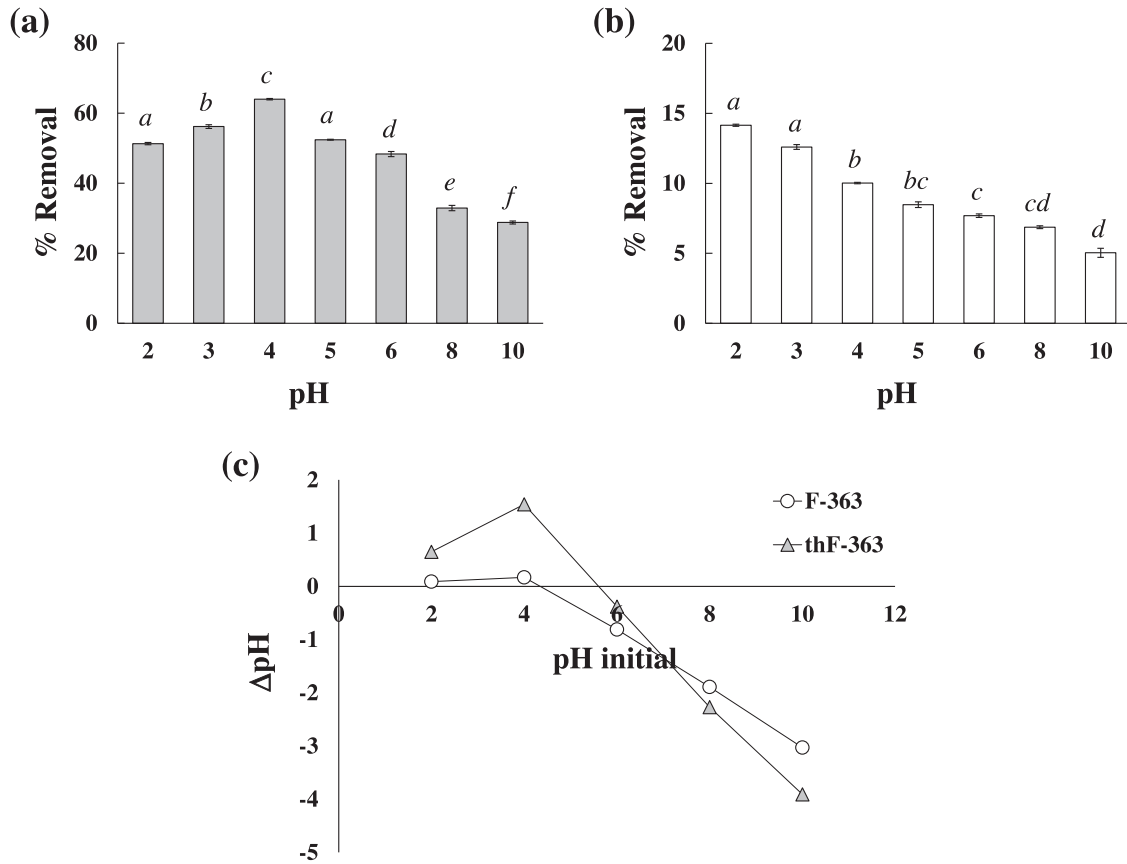


Figure 2. Effect of solution pH on Pi adsorption onto (a) thF-363 and (b) F-363. (c) The pH of point of zero charge of thF-363 and F-363. Data are means \pm SD from three replicates. Different lowercase letters above the graph bars denote significant differences among different pH (ANOVA and Tukey's test, $p < 0.05$).

explained by observing the pH_{PZC} of thF-363 and F-363 adsorbent. As shown in Figure 2c, the pH_{PZC} value for thF-363 and F-363 is 5.6 and 4.4, respectively. The pH_{PZC} value indicates the surface charge tendency of the adsorbent; positive surface charge occurs at pH solution $<$ pH_{PZC} , while negative surface charge occurs at pH solution $>$ pH_{PZC} [55].

The interaction of Pi and thF-363 at acidic and basic pH is illustrated in Figure 3. At acidic pH (i.e., pH solution $<$ pH_{PZC}), thF-363 particles are positively charged while Pi dominantly presents as

negatively charged species (H_2PO_4^-) [56]. The opposite charges between the adsorbent and adsorbate generate electrostatic attraction, which promotes the adsorption of Pi onto the adsorbent surface. At basic pH (i.e., pH solution $>$ pH_{PZC}), thF-363 tends to be negatively charged; and, Pi dominantly occurs as negatively charged species of HPO_4^{2-} [56]. The same charges between thF-363 and Pi lead to repulsion force, which demotes the adsorption of Pi. A similar effect of surface charge on the adsorption performance of adsorbent has also been reported in other works [46,57,58]. For example, Jiang et al. [57]

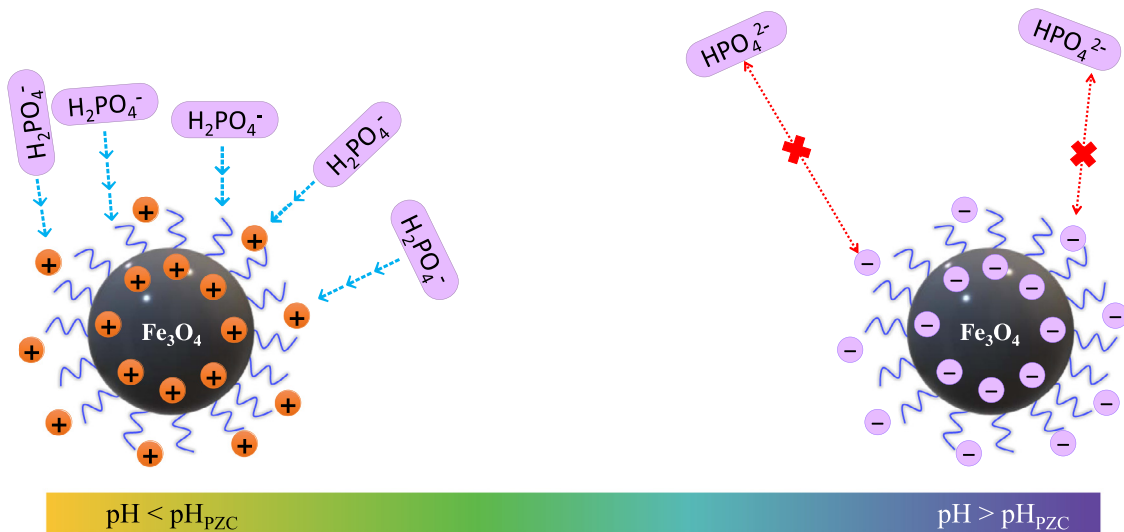


Figure 3. Illustration on the effect of pH, adsorbent surface charge, and adsorbate species distribution on the thF-363 and Pi interaction.

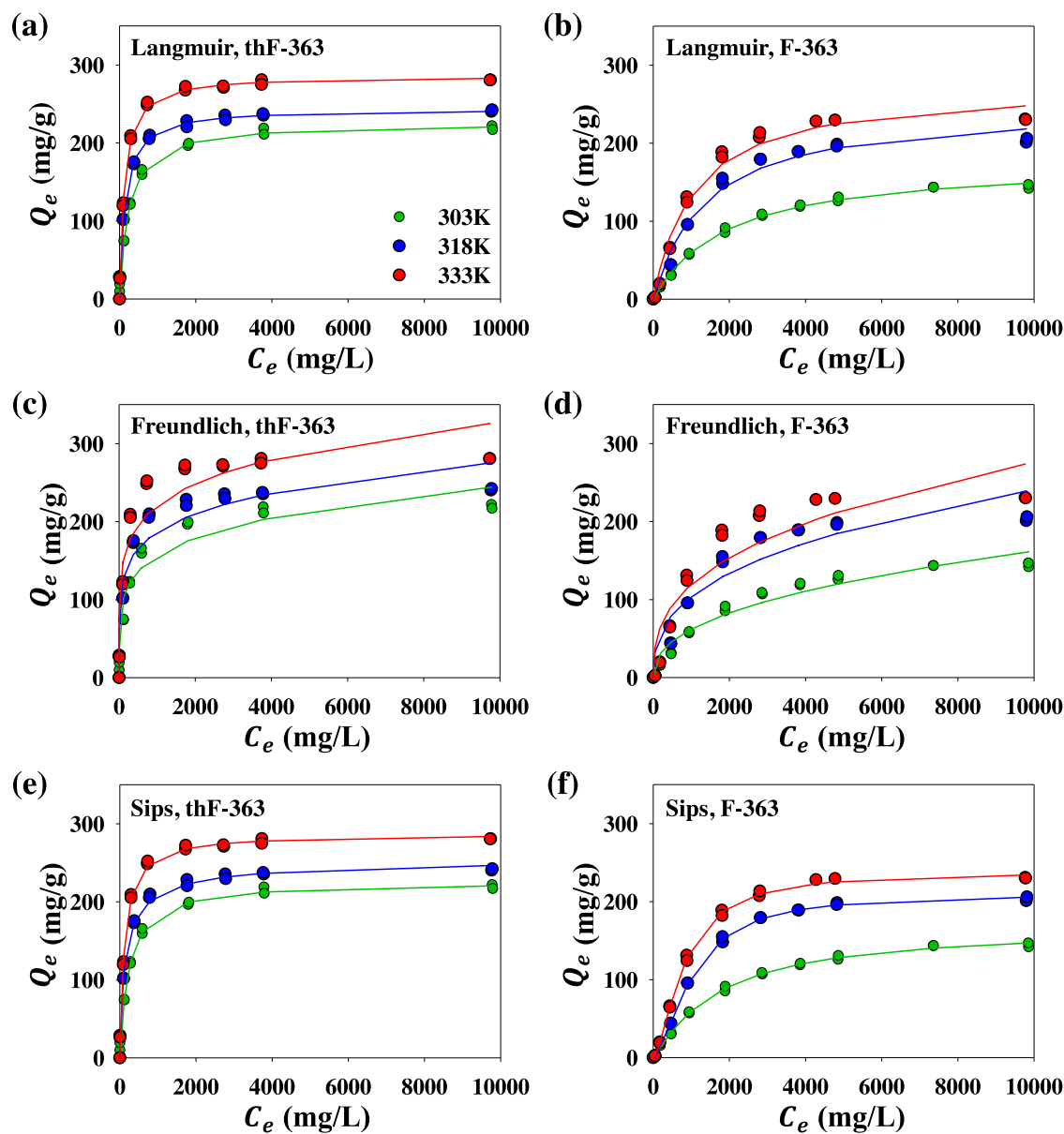


Figure 4. Isotherm data of Pi adsorption on (a,c,e) thF-363 and (b,d,f) F-363 at three different adsorption temperatures (303 K, green; 318 K, blue; and 333 K, red symbols). The experiments were done in triplicate. The lines represent the (a, b) Langmuir, (c, d) Freundlich, and (e,f) Sips data fitting.

reported that the Fe_3O_4 particles were negatively charged at pH 7, which led to the electrostatic adsorption between the particles and positively charged anthocyanin. In addition, the occurrence of excess hydroxyl ions also may act as competing molecules and occupy the adsorption site of Pi anions on the adsorbent [59].

3.3. Adsorption isotherm of Pi onto thF-363 magnetic adsorbent

The adsorption isotherm plays a crucial role in determining the maximum adsorption capacity and estimating the adsorption mechanism of adsorbents. The isotherm study of Pi on thF-363 and F-363 was conducted at adsorption temperatures of 303, 318, and 333 K (Figure 4). At any given temperature, the system containing thF-363 displayed typical H-adsorption curves, which suggests that the adsorption was driven by the electrostatic forces due to different charges of adsorbate and adsorbent. While for F-363 adsorbent, the system shows an L-type curve which commonly occurs in the adsorption of ions in aqueous solutions and the adsorption process is driven

by van der Waals forces [60]. Overall, the adsorption process with an adsorbent plateau at high adsorbate concentration follows the subclass classification number 2, demonstrating the absence of the intermolecular forces between the adsorbed-adsorbate molecules and the adsorbate molecules in bulk solution [61]. Both thF-363 and F-363 tend to exhibit endothermic adsorption behavior, where the equilibrium adsorption capacity (Q_e) increases with temperature.

Three isotherm models, Langmuir, Freundlich, and Sips, were used to evaluate the adsorption behavior of Pi onto magnetite sorbent thF-363 and F-363; the calculated parameters of NLR fitting the isotherm models are listed in Table 2. The NLR fitting method was chosen as the best regression method since it gave the smallest SSE value and the closest fitting to the experimental data compared to LR and ODR methods (Tables S1, S2, and Figures S3, S4). The Sips model showed the best fitting with the experimental data of both thF-363 ($R_{adj}^2 = 0.988-0.994$) and F-363 ($R_{adj}^2 = 0.997-0.999$). The goodness of fitting also is displayed on the value of calculated Q_S from the Sips model, which showed the closest resemblance to the Q_{exp} . The Sips

Table 2

Adsorption isotherm parameters of Pi adsorption on either thF-363 or F-363 obtained from nonlinear regression fitting using Langmuir, Freundlich, and Sips models.

Model	Parameter (Unit)	thF-363			F-363		
		303 K	318 K	333 K	303 K	318 K	333 K
Langmuir	Q_{exp} (mg/g)	221.993	242.281	280.954	146.977	206.093	230.923
	Q_L (mg/g)	226.051	243.906	286.376	177.699	248.289	275.639
	K_L (L/mg)	0.0042	0.0072	0.0086	0.0005	0.0007	0.0009
	R_L	0.02–0.83	0.01–0.74	0.01–0.70	0.17–0.98	0.13–0.97	0.1–0.96
	R^2	0.994	0.987	0.994	0.997	0.982	0.983
	R_{adj}^2	0.993	0.986	0.994	0.997	0.980	0.981
Freundlich	SSE	559.782	1443.821	911.814	139.427	1811.293	2575.329
	K_F (mg/g)(L/mg) ⁻ⁿ	39.190	57.528	67.881	3.519	8.388	9.833
	n_F	5.017	5.866	5.854	2.404	2.743	2.752
	R^2	0.938	0.923	0.886	0.951	0.894	0.875
	R_{adj}^2	0.933	0.918	0.879	0.948	0.887	0.868
	SSE	5553.256	8802.450	18520.144	2232.027	10464.750	17976.803
Sips	Q_S (mg/g)	225.837	257.013	287.680	168.019	209.278	238.421
	K_S (L/g)	0.004	0.025	0.010	0.0003	0.00001	0.00002
	n_S	1.005	0.748	0.967	1.108	1.695	1.594
	R^2	0.994	0.989	0.994	0.998	0.999	0.999
	R_{adj}^2	0.993	0.988	0.994	0.997	0.999	0.999
	SSE	559.683	1211.164	905.877	101.864	70.988	156.020

model also can be used to confirm the satisfactory of the Langmuir or Freundlich fitting. Based on the fitting results, the n_S value of all the adsorption systems is close to 1, indicating their better approach to the Langmuir model. Furthermore, the K_S of the Sips model does not show zero value, which confirms the Langmuir approach [35,62].

In agreement with the Sips fitting result, the Langmuir model showed better fitting with the experimental data for both adsorbents, while the fitting with Freundlich model tends to deviate strongly from the experimental data. Based on the Langmuir isotherm, the maximum adsorption capacity of Pi increased from 226.051 to 286.376 mg/g for thF-363 and 177.699 to 275.639 mg/g for F-363 at the increasing adsorption temperature. Proportionally, the equilibrium constant K_L value also increased at higher temperature. On the other hand, the favorability of adsorbent towards Pi was evaluated by the value of the separation factor constant (R_L) which can be obtained from Langmuir model. The value of R_L of all adsorption experiments showed the value between 0 and 1, indicating that the synthesized adsorbents were all suitable for the Pi adsorption [63]. Disregards of the data fitting, the n_F values of both samples fallen within the 2–10 range which indicate the adsorption is favorable [63]. It is also worth mentioning that the thF-363 showed substantially higher adsorption capacity compared to F-363; up to 1.51-fold higher capacity for adsorption at 303K.

The mechanism of Pi adsorption on F-363 and thF-363 is illustrated in Figure 5. The adsorption of Pi on F-363 was driven by the electrostatic attraction between the anionic species of Pi and positively charged F-363, which is a typical phenomenon observed in the adsorption of anionic Pi onto iron oxides-based sorbents [64,65]. Distinctively, the enhanced adsorption capacity in thF-363 adsorbent may be attributed to the presence of thiamine, which provides additional amino ($-NH_2$) binding sites. The high Pi adsorption on the $-NH_2$ functionalized adsorbents has been reported in several works [66–68], wherein the anionic Pi establishes electrostatic attraction with the protonated species of the $-NH_2$ functional group.

Pi removal through adsorption method had been previously studied using various magnetite-based adsorbents [66,68–71]. A comparison of the maximum Pi adsorption capacities onto thF-363, F-363, and other magnetite composite adsorbents is presented in Table 3. The capacity of thF-363 for Pi adsorption is significantly higher than other reported magnetite adsorbents, which show the superiority of thF-363 adsorbent.

3.4. Adsorption thermodynamic

Thermodynamic parameters can be used to estimate the characteristics of Pi adsorption onto the adsorbent surface. Figure 6 shows the adsorption thermodynamic of the adsorbents. The negative ΔG°

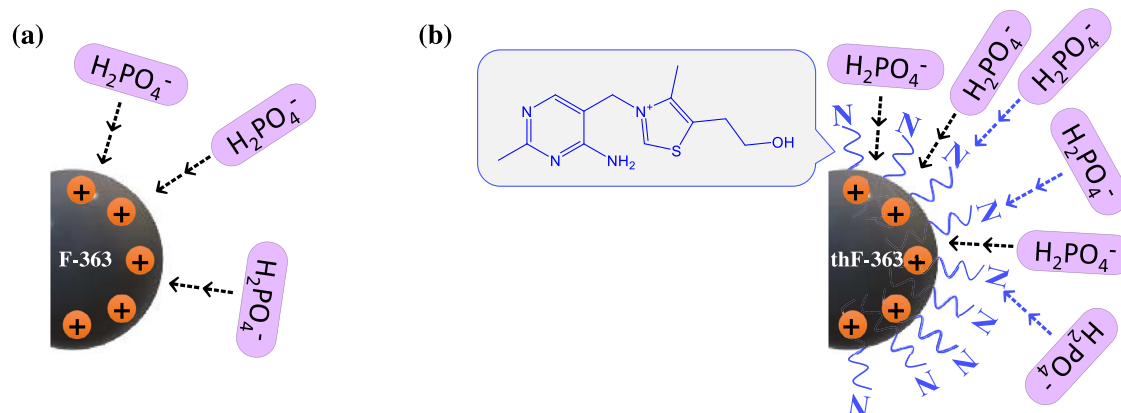


Figure 5. Possible mechanism of Pi adsorption on (a) F-363 and (b) thF-363.

Table 3

Comparison of Pi adsorption capacities and optimum adsorption condition of thF-363, F-363, and previously reported magnetite-based adsorbents.

Adsorbent	Conditions	Q_{max} (mg/g)	References
thF-363	pH 4, 333 K	287.7	This study
F-363	pH 3, 333 K	238.4	This study
Fe ₃ O ₄ /ZrO ₂ /chitosan	pH 3, 298 K	26.5	[68]
Fe ₃ O ₄ @LDH composites	pH 3	26.5–36.9	[69]
Fe ₃ O ₄ @alkali-treated calcium-silicate	pH 8, 298 K	128	[70]
Chitosan/Al ₂ O ₃ /Fe ₃ O ₄ nanofiber	pH 3, 303 K	130.9	[66]
Rectorite/Fe ₃ O ₄ -CTAB	pH 5, 303 K	174.5	[71]

value at all given temperatures demonstrate the thermodynamically favorable and spontaneous adsorption of Pi onto the thF-363 and F-363 surface. Specifically -26.22, -28.47, and -30.72 kJ/mol for the ΔG^0 of thF-363 at 303, 318, and 333 K, and ΔG -20.83, -22.67, and -24.52 kJ/mol for F-363 at 303, 318, and 333 K. The ΔH for each temperature increase was evaluated to observe the heat transfer direction in the adsorption system. Positive ΔH values obtained in the Pi–thF-363 system was 27.66 kJ/mol, 10.24 kJ/mol and 19.23 kJ/mol when the adsorption temperature was increased from 303 to 318K, 318 to 333 K, and 303 to 333 K, respectively. The same positive values of ΔH were calculated from the system containing F-363 as well (ΔH = 18.84 kJ/mol for 303 → 318 K, 13.89 kJ/mol for 318 → 333 K, and 16.44 kJ/mol for

303 → 333 K). These positive ΔH values indicate that the adsorption process happens endothermically and favors high temperature [58,72], as confirmed by the maximum adsorption capacity increase when the temperature increases from 303 to 333 K (Table 2).

The ΔS value for each temperature increase was also calculated. A positive value of ΔS was found at each temperature increase. For instance, the ΔS = 0.178 kJ/mol·K and 0.150 kJ/mol·K when the adsorption temperature in Pi–thF-363 system increased from 303 to 318K and 303 to 333K, respectively. In the system containing F-363, the $\Delta S_{303 \rightarrow 318}$ was 0.131 kJ/mol·K and $\Delta S_{303 \rightarrow 333}$ is 0.123 kJ/mol·K. The positive ΔS values indicate the increase in the disorder of ions in the adsorbate-adsorbent interface along with the increase in temperature [63,73].

3.5. Environmental compatibility assessment of thF-363 on plant growth

The usage of non-environmentally friendly adsorbents for contaminant removal from wastewater may evoke ecological risk toward soils, plants, and their surrounding ecosystem. To evaluate the environmental compatibility of thF-363, this work focused on its effect on the overall growth of *A. thaliana* seedlings upon supplementation to plant growth media. The evaluation was based on phenotypical observation of the seedling aerial and root development. Figure 7a

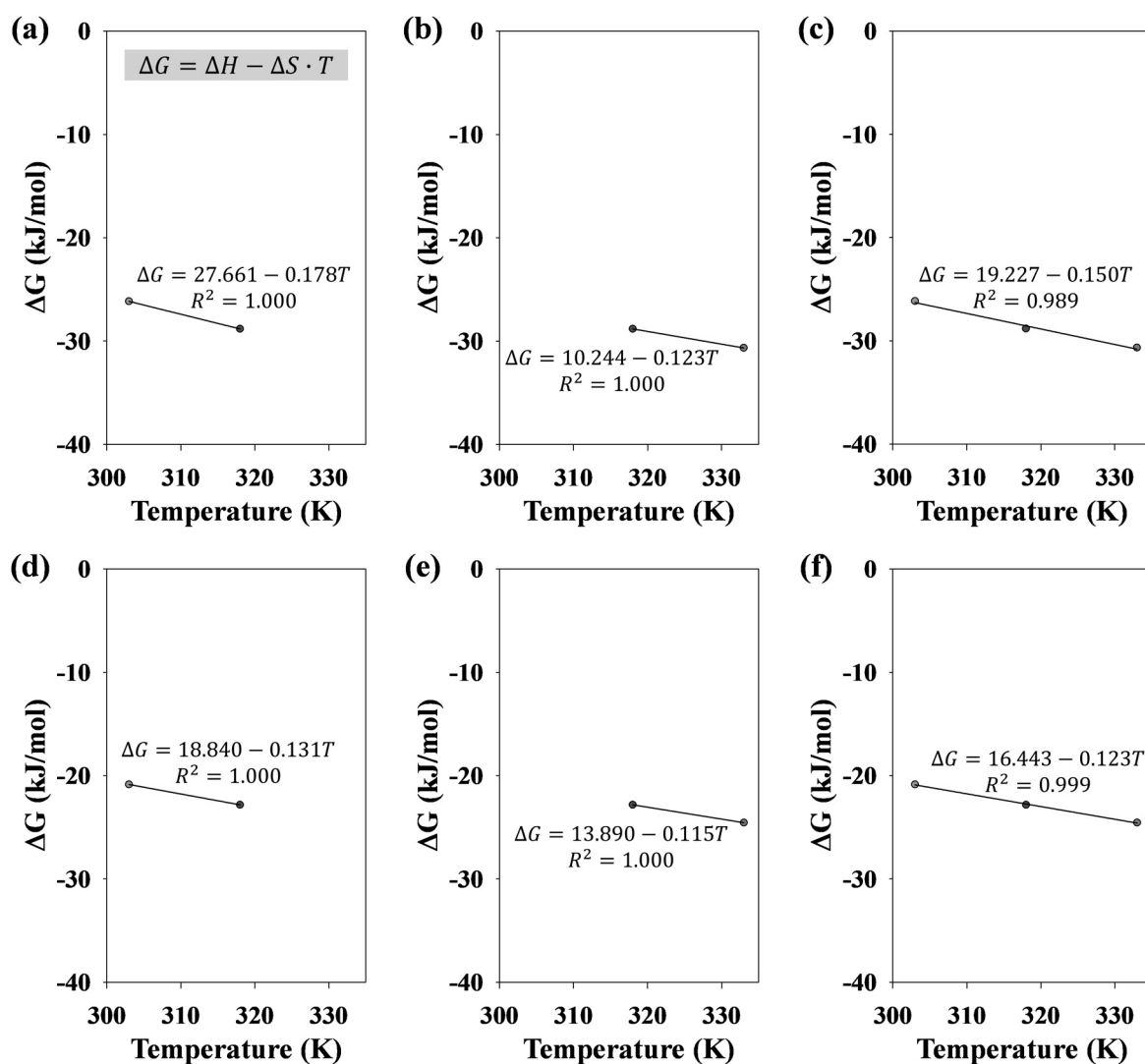


Figure 6. Adsorption thermodynamics for the removal of Pi by (a-c) thF-363 and (d-f) F-363.

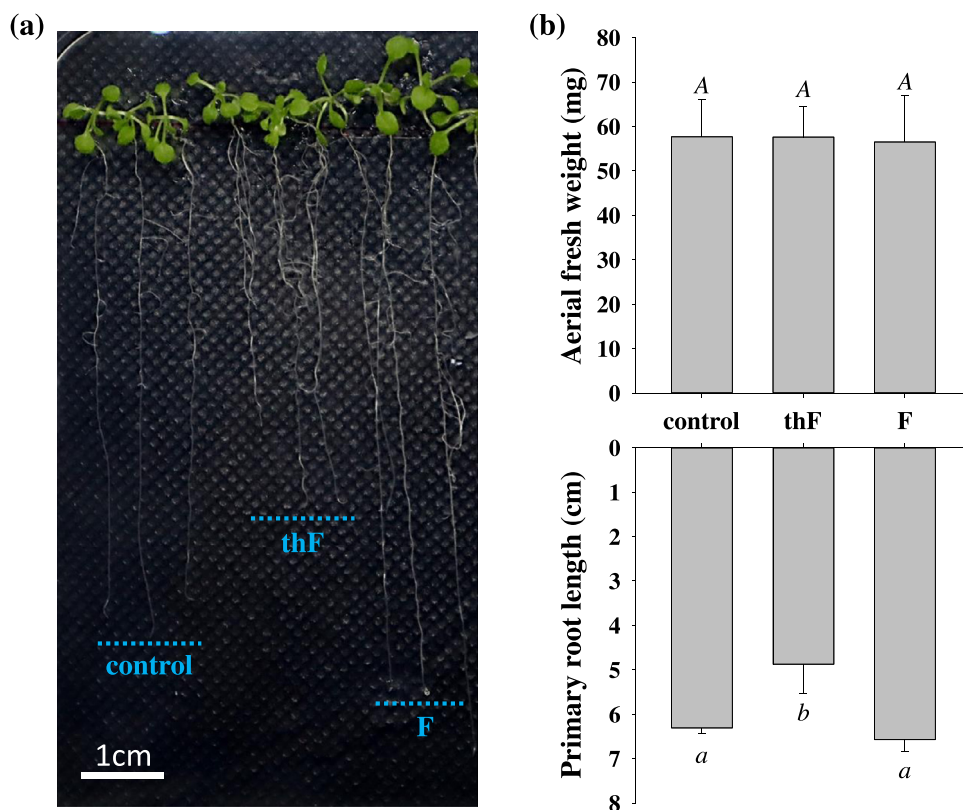


Figure 7. Growth observation of *Arabidopsis thaliana* seedlings grown on supplemented media. (a) Image of 14-day-old seedlings. (b) Aerial fresh weight (upper panel) and primary root length (lower panel) of the seedlings. Data are means \pm SD from three replicates, with 8 seedlings observed per replicate. Different letters above and below the graph bars denote significant differences among different growth media (ANOVA and Tukey's test, $p < 0.05$).

shows the representative 14-day-old seedlings grown on basal (control), thF-363 supplemented (thF), and F-363 supplemented (F) media. The measured aerial fresh weight and primary root length of the seedlings are presented in Figure 7b. No observable difference can be seen between the aerial fresh weight of seedlings grown on the thF, F, and control. However, the thF-363 supplementation slightly affects the primary root growth of the seedlings (Figure 7b, lower panel). This phenomenon might be due to the high adsorption capacity of freshly synthesized thF-363, which reduces nutrient availability in the media, thus inhibiting root growth. Nevertheless, both modified and unmodified Fe_3O_4 caused minimal to no adverse effects on phenotypical growth of seedlings' root and aerial tissues, which suggest their non-phytotoxic properties.

4. Conclusion

An environmentally friendly adsorbent with high adsorption capacity toward phosphate ions (Pi), namely thiamine-functionalized Fe_3O_4 (thF), was successfully synthesized through *in-situ* reaction by combining $\text{NH}_4\text{OH}:\text{Fe}:\text{thiamine}$ at a molar ratio of 10:1:1 and a temperature of 363 K. Detailed characterization through XRD, XPS, FTIR, SQUID, and N_2 adsorption-desorption isotherm confirmed the formation of Fe_3O_4 , the incorporation of thiamine, and gave insight on the other physicochemical properties of the thF-363. The thiamine functionalization was shown to substantially increase the adsorption capacity for Pi removal up to 1.51-fold (at 303 K) compared to the unmodified Fe_3O_4 . The improved adsorption capacity is attributed to the synergistic effect of the surface charge, area, and the occurrence of the thiamine functional group in thF-363. The adsorption process fitted well with the Langmuir and Sips isotherm model, with a maximum adsorption capacity of 287.680 mg/g at 333 K. The Pi adsorption to the adsorbents followed endothermic and spontaneous

mechanisms. Both modified and unmodified Fe_3O_4 showed a non-toxic effect on plant growth, confirming their environmentally-friendly nature.

Author Contribution

A.E.A. Conceptualization; Data curation; Funding acquisition; Investigation; Writing. Y.N.T.-C. Formal analysis; Investigation; Methodology; Visualization; Writing. Q.N.H. Formal analysis; Investigation; Methodology. P.L.T.-N. Funding acquisition; Supervision; Project administration. S.P.S., and A.W.G. Supervision; Project administration; Resources. V.B. Formal analysis. H.-Y. H and Y.-H.J. Supervision; Resources.

Declaration of Competing Interest

The authors declare that the research was conducted without any commercial or financial relationships that could be construed as a potential conflict of interest.

Acknowledgments

This research was funded by Vietnam National Foundation for Science and Technology Development (NAFOSTED) under Grant Number 103.02-2020.64 to P.L. Tran-Nguyen. A. E. Angkawijaya is supported by the Ministry of Science and Technology (MOST 109-2221-E-011-058 and MOST 110-2221-E-011-018) and the National Taiwan University of Science and Technology (101H451403). S.P. Santoso is supported by Widya Mandala Surabaya Catholic University through an Internal Research Grant.

Supplementary materials

Supplementary material associated with this article can be found in the online version at doi:10.1016/j.jtice.2021.104162.

References

- Jordan RM, Myers VS, Yoho B, Spurrell FA. Effect of Calcium and Phosphorus Levels on Growth, Reproduction and Bone Development of Ponies. *J Anim Sci* 1975;40(1):78–85.
- Chaudhary MI, Adu-Gyamfi JJ, Saneoka H, Nguyen NT, Suwa R, Kanai S, et al. The effect of phosphorus deficiency on nutrient uptake, nitrogen fixation and photosynthetic rate in mungbean, mungbean and soybean. *Acta Physiologica Plantarum* 2008;30(4):537–44.
- Angkawijaya AE, Nguyen VC, Nakamura Y. Enhanced root growth in phosphate-starved Arabidopsis by stimulating de novo phospholipid biosynthesis through the overexpression of *LYSOPHOSPHATIDIC ACID ACYLTRANSFERASE 2 (LPAT2)*. *Plant, Cell & Environment* 2017;40(9):1807–18.
- Wang GC. 4 - Nonmetallurgical slags editor. In: Wang GC, editor. *The Utilization of Slag in Civil Infrastructure Construction*. Woodhead Publishing; 2016. p. 63–85.
- USGS. Phosphate rock editor. In: *Summaries MC, editor. Phosphate Rock Statistics and Information*. U.S Geological Survey; 2021 <https://pubs.usgs.gov/periodicals/mcs2021/mcs2021-phosphate.pdf>.
- Aleweli C, Ringeval B, Ballabio C, DA Robinson, Panagos P, Borrelli P. Global phosphorus shortage will be aggravated by soil erosion. *Nature Communications* 2020;11(1):4546.
- Hua K, Zhu B. Phosphorus loss through surface runoff and leaching in response to the long-term application of different organic amendments on sloping croplands. *J Soils Sed* 2020;20(9):3459–71.
- Diaz RJ, Rosenberg R. Spreading Dead Zones and Consequences for Marine Ecosystems. *Science* 2008;321(5891):926–9.
- Huang H, Liu J, Zhang P, Zhang D, Gao F. Investigation on the simultaneous removal of fluoride, ammonia nitrogen and phosphate from semiconductor wastewater using chemical precipitation. *Chem Eng J* 2017;307:696–706.
- Bui TH, Hong SP, Kim C, Yoon J. Performance analysis of hydrated Zr (IV) oxide nanoparticle-impregnated anion exchange resin for selective phosphate removal. *Journal of Colloid and Interface Science* 2021;586:741–7.
- Bui TH, Hong SP, Yoon J. Development of nanoscale zirconium molybdate embedded anion exchange resin for selective removal of phosphate. *Water research* 2018;134:22–31.
- Bektaş N, Akbulut H, Inan H, Dimoglo A. Removal of phosphate from aqueous solutions by electro-coagulation. *J Hazard Mater* 2004;106(2–3):101–5.
- Hashim KS, Al Khaddar R, Jasim N, Shaw A, Phipps D, Kot P, et al. Electrocoagulation as a green technology for phosphate removal from River water. *Separation and Purification Technology* 2019;210:135–44.
- Lin J-Y, Kim M, Li D, Kim H, Huang C-p. The removal of phosphate by thermally treated red mud from water: The effect of surface chemistry on phosphate immobilization. *Chemosphere* 2020;247:125867.
- dos Reis GS, Thue PS, Cazaciu BG, Lima EC, Sampaio CH, Quattrone M, et al. Effect of concrete carbonation on phosphate removal through adsorption process and its potential application as fertilizer. *Journal of Cleaner Production* 2020;256:120416.
- Tanada S, Kabayama M, Kawasaki N, Sakiyama T, Nakamura T, Araki M, et al. Removal of phosphate by aluminum oxide hydroxide. *Journal of colloid and interface science* 2003;257(1):135–40.
- Zhu D, Chen Y, Yang H, Wang S, Wang X, Zhang S, et al. Synthesis and characterization of magnesium oxide nanoparticle-containing biochar composites for efficient phosphorus removal from aqueous solution. *Chemosphere* 2020;247:125847.
- Das TK, Scott Q, Bezbaruah AN. Montmorillonite-iron crosslinked alginate beads for aqueous phosphate removal. *Chemosphere* 2021;281:130837.
- Abdellaoui Y, Abou Oualid H, Hsini A, El Ibrahim B, Laabd M, El Ouardi M, et al. Synthesis of zirconium-modified Merlinoite from fly ash for enhanced removal of phosphate in aqueous medium: Experimental studies supported by Monte Carlo/SA simulations. *Chem Eng J* 2021;404:126600.
- Yoon S-Y, Lee C-G, Park J-A, Kim J-H, Kim S-B, Lee S-H, et al. Kinetic, equilibrium and thermodynamic studies for phosphate adsorption to magnetic iron oxide nanoparticles. *Chem Eng J* 2014;236:341–7.
- Wang S, Bian S, Liu J, Li J, Xu S, Liang Z. Highly adsorptive pristine and magnetic biochars prepared from crayfish shell for removal of Cu(II) and Pb(II). *Journal of the Taiwan Institute of Chemical Engineers* 2021;127:175–85.
- Zhang Z, Yang G, Wu J, He J-S, Zhang Y-Z, Tian D, et al. Enhanced properties of magnetic ultralight pear sponge assisted by Fenton-like reaction for oil-water separation. *Journal of the Taiwan Institute of Chemical Engineers* 2021;126:332–40.
- Fatima H, Lee D-W, Yun HJ, Kim K-S. Shape-controlled synthesis of magnetic Fe₃O₄ nanoparticles with different iron precursors and capping agents. *RSC advances* 2018;8(41):22917–23.
- Lu W, Shen Y, Xie A, Zhang W. Green synthesis and characterization of superparamagnetic Fe₃O₄ nanoparticles. *J Magn Magn Mater* 2010;322(13):1828–33.
- Veloso SR, Ferreira PM, Martins JA, Coutinho PJ, Castanheira E. Magnetogels: Prospects and main challenges in biomedical applications. *Pharmaceutics* 2018;10(3):145.
- Wu W, Jiang C, Roy VA. Recent progress in magnetic iron oxide–semiconductor composite nanomaterials as promising photocatalysts. *Nanoscale* 2015;7(1):38–58.
- Pourcel L, Moulin M, Fitzpatrick TB. Examining strategies to facilitate vitamin B1 biofortification of plants by genetic engineering. *Frontiers in plant science* 2013;4:160.
- Tunc-Ozdemir M, Miller G, Song L, Kim J, Sodek A, Koussevitzky S, et al. Thiamin confers enhanced tolerance to oxidative stress in Arabidopsis. *Plant physiology* 2009;151(1):421–32.
- Asensi-Fabado MA, Munné-Bosch S. Vitamins in plants: occurrence, biosynthesis and antioxidant function. *Trends in plant science* 2010;15(10):582–92.
- Yusof ZNB. Thiamine and its role in protection against stress in plants (enhancement in thiamine content for nutritional quality improvement). *Nutritional Quality Improvement in Plants*. Springer; 2019. p. 177–86.
- Tomlinson RV, Kuhlman DP, Torrence PF, Tieckelmann H. Precursors of the pyrimidine and thiazole rings of thiamine. *Biochimica et Biophysica Acta (BBA) - General Subjects* 1967;148(1):1–10.
- Naeimi H, Ansarian Z. Effective preparation of amine-functionalized nano magnetite as a precursor of novel solid acid catalyst for one-pot synthesis of xanthenes under solvent-free conditions. *Journal of the Taiwan Institute of Chemical Engineers* 2018;85:265–72.
- Lin Y-F, Chen H-W, Chen Y-C, Chiou C-S. Application of magnetite modified with polyacrylamide to adsorb phosphate in aqueous solution. *Journal of the Taiwan Institute of Chemical Engineers* 2013;44(1):45–51.
- Yin Z, Zhu L, Mo F, Li S, Hu D, Chu R, et al. Preparation of biochar grafted with amino-riched dendrimer by carbonization, magnetization and functional modification for enhanced copper removal. *Journal of the Taiwan Institute of Chemical Engineers* 2021;121:349–59.
- Santoso SP, Bundjaja V, Angkawijaya AE, Gunarto C, Go AW, Yuliana M, et al. One-step synthesis of nitrogen-grafted copper-gallic acid for enhanced methylene blue removal. *Scientific reports* 2021;11(1):12021.
- Lowry OH, Lopez JA. The determination of inorganic phosphate in the presence of labile phosphate esters. *The Journal of biological chemistry* 1946;162:421–8.
- Shahryari Z, Goharizi AS, Azadi M. Experimental study of methylene blue adsorption from aqueous solutions onto carbon nano tubes. *International Journal of Water Resources and Environmental Engineering* 2010;2147483647(2):016–28.
- Saruchi Kumar V. Adsorption kinetics and isotherms for the removal of rhodamine B dye and Pb²⁺ ions from aqueous solutions by a hybrid ion-exchanger. *Arab J Chem* 2019;12(3):316–29.
- El-Khaiary MI. Least-squares regression of adsorption equilibrium data: Comparing the options. *J Hazard Mater* 2008;158(1):73–87.
- Cantrell CA. Technical Note: Review of methods for linear least-squares fitting of data and application to atmospheric chemistry problems. *Atmos Chem Phys* 2008;8(17):5477–87.
- Lima EC, Gomes AA, Tran HN. Comparison of the nonlinear and linear forms of the van't Hoff equation for calculation of adsorption thermodynamic parameters (ΔS° and ΔH°). *J Mol Liq* 2020;311:113315.
- Lima EC, Hosseini-Bandegharaei A, Moreno-Piraján JC, Anastopoulos I. A critical review of the estimation of the thermodynamic parameters on adsorption equilibria. Wrong use of equilibrium constant in the Van't Hoff equation for calculation of the thermodynamic parameters of adsorption. *J Mol Liq* 2019;273:425–34.
- Santoso SP, Angkawijaya AE, Yuliana M, Bundjaja V, Soetaredjo FE, Ismadji S, et al. Saponin-intercalated organoclays for adsorptive removal of β -carotene: Equilibrium, reusability, and phytotoxicity assessment. *Journal of the Taiwan Institute of Chemical Engineers* 2020;117:198–208.
- Estelle MA, Somerville C. Auxin-resistant mutants of Arabidopsis thaliana with an altered morphology. *Mol Gen Genet* 1987;206:200–6.
- Nakamura Y, Awai K, Masuda T, Yoshioka Y, Takamiya K-i, Ohta H. A Novel Phosphatidylcholine-hydrolyzing Phospholipase C Induced by Phosphate Starvation in Arabidopsis. *J Biol Chem* 2005;280:7469–76.
- Angkawijaya AE, Santoso SP, Bundjaja V, Soetaredjo FE, Gunarto C, Ayucitra A, et al. Studies on the performance of bentonite and its composite as phosphate adsorbent and phosphate supplementation for plant. *J Hazard Mater* 2020;399:123130.
- Bunzen H, Grzywa M, Hambach M, Spirkl S, Volkmer D. From Micro to Nano: A Toolbox for Tuning Crystal Size and Morphology of Benzotriazole-Based Metal–Organic Frameworks. *Crystal Growth & Design* 2016;16(6):3190–7.
- Dong M, Miao X, Brisse R, Deng W, Jousselme B, Silly F. Molecular trapping in two-dimensional chiral organic Kagomé nanoarchitectures composed of Baravelle spiral triangle enantiomers. *NPG Asia Materials* 2020;12(1):20.
- Owusu KA, Qu L, Li J, Wang Z, Zhao K, Yang C, et al. Low-crystalline iron oxide hydroxide nanoparticle anode for high-performance supercapacitors. *Nature Communications* 2017;8(1):14264.
- Mohapatra J, Mitra A, Tyagi H, Bahadur D, Aslam M. Iron oxide nanorods as high-performance magnetic resonance imaging contrast agents. *Nanoscale* 2015;7(20):9174–84.
- Grosvenor A, Kobe B, Biesinger M, McIntyre N. Investigation of multiplet splitting of Fe 2p XPS spectra and bonding in iron compounds. *Surface and Interface Analysis: An International Journal devoted to the development and application of techniques for the analysis of surfaces, interfaces and thin films* 2004;36(12):1564–74.
- Yamashita T, Hayes P. Analysis of XPS spectra of Fe²⁺ and Fe³⁺ ions in oxide materials. *Applied surface science* 2008;254(8):2441–9.
- Sing KS. Reporting physisorption data for gas/solid systems with special reference to the determination of surface area and porosity (Recommendations 1984). *Pure Appl Chem* 1985;57(4):603–19.

- [54] Zhang J, Han J, Wang M, Guo R. Fe₃O₄/PANI/MnO₂ core-shell hybrids as advanced adsorbents for heavy metal ions. *J Mater Chem A* 2017;5(8):4058–66.
- [55] Gulicovski JJ, Cerović LS, Milonjić SK. Point of Zero Charge and Isoelectric Point of Alumina. *Mater Manuf Processes* 2008;23(6):615–9.
- [56] Havlin JL, Schlegel AJ. Review of Phosphite as a Plant Nutrient and Fungicide 2021;5(3):52.
- [57] Jiang X, Guan Q, Feng M, Wang M, Yan N, Wang M, et al. Preparation and pH Controlled Release of Fe₃O₄/Anthocyanin Magnetic Biocomposites 2019;11(12):2077.
- [58] Andreas A, Winata ZG, Santoso SP, Angkawijaya AE, Yuliana M, Soetaredjo FE, et al. Biocomposite hydrogel beads from glutaraldehyde-crosslinked phytochemicals in alginate for effective removal of methylene blue. *J Mol Liq* 2021;329:115579.
- [59] Chubar N, Kanibolotskyy V, Strelko V, Gallios G, Samanidou V, Shaposhnikova T, et al. Adsorption of phosphate ions on novel inorganic ion exchangers. *Colloids Surf Physicochem Eng Aspects* 2005;255(1–3):55–63.
- [60] Giles CH, MacEwan TH, Nakhwa SN, Smith D. 786. Studies in adsorption. Part XI. A system of classification of solution adsorption isotherms, and its use in diagnosis of adsorption mechanisms and in measurement of specific surface areas of solids. *J Chem Soc* 1960(0):3973–93.
- [61] Piccin JS, Cadaval TRSA, de Pinto LAA, Dotto GL. Adsorption Isotherms in Liquid Phase: Experimental, Modeling, and Interpretations editors. In: Bonilla-Petriciolet A, Mendoza-Castillo DI, Reynel-Ávila HE, editors. *Adsorption Processes for Water Treatment and Purification*. Cham: Springer International Publishing; 2017. p. 19–51.
- [62] Al-Ghouti MA, Da'ana DA. Guidelines for the use and interpretation of adsorption isotherm models: A review. *J Hazard Mater* 2020;393:122383.
- [63] Tanhaei B, Ayati A, Lahtinen M, Sillanpää M. Preparation and characterization of a novel chitosan/Al₂O₃/magnetite nanoparticles composite adsorbent for kinetic, thermodynamic and isotherm studies of Methyl Orange adsorption. *Chem Eng J* 2015;259:1–10.
- [64] Ajmal Z, Muhmood A, Usman M, Kizito S, Lu J, Dong R, et al. Phosphate removal from aqueous solution using iron oxides: adsorption, desorption and regeneration characteristics. *Journal of colloid and interface science* 2018;528:145–55.
- [65] Zeng H, Fisher B, Giammar DE. Individual and competitive adsorption of arsenate and phosphate to a high-surface-area iron oxide-based sorbent. *Environ Sci Technol* 2008;42(1):147–52.
- [66] Bozorgpour F, Ramandi HF, Jafari P, Samadi S, Yazd SS, Aliabadi M. Removal of nitrate and phosphate using chitosan/Al₂O₃/Fe₃O₄ composite nanofibrous adsorbent: comparison with chitosan/Al₂O₃/Fe₃O₄ beads. *International journal of biological macromolecules* 2016;93:557–65.
- [67] Shen H, Wang Z, Zhou A, Chen J, Hu M, Dong X, et al. Adsorption of phosphate onto amine functionalized nano-sized magnetic polymer adsorbents: mechanism and magnetic effects. *RSC Advances* 2015;5(28):22080–90.
- [68] Jiang H, Chen P, Luo S, Tu X, Cao Q, Shu M. Synthesis of novel nanocomposite Fe₃O₄/ZrO₂/chitosan and its application for removal of nitrate and phosphate. *Applied Surface Science* 2013;284:942–9.
- [69] Yan L-g, Yang K, Shan R-r, Yan T, Wei J, Yu S-j, et al. Kinetic, isotherm and thermodynamic investigations of phosphate adsorption onto core-shell Fe₃O₄@LDHs composites with easy magnetic separation assistance. *Journal of colloid and interface science* 2015;448:508–16.
- [70] Jiang D, Amano Y, Machida M. Removal and recovery of phosphate from water by a magnetic Fe₃O₄@ASC adsorbent. *Journal of environmental chemical engineering* 2017;5(5):4229–38.
- [71] Wang F, Liu D, Zheng P, Ma X. Synthesis of rectorite/Fe₃O₄-CTAB composite for the removal of nitrate and phosphate from water. *Journal of Industrial and Engineering Chemistry* 2016;41:165–74.
- [72] Hu D, Wang L. Adsorption of amoxicillin onto quaternized cellulose from flax noil: Kinetic, equilibrium and thermodynamic study. *Journal of the Taiwan Institute of Chemical Engineers* 2016;64:227–34.
- [73] Liu X, Tian J, Li Y, Sun N, Mi S, Xie Y, et al. Enhanced dyes adsorption from wastewater via Fe₃O₄ nanoparticles functionalized activated carbon. *J Hazard Mater* 2019;373:397–407.